



In vivo acoustoelectric imaging for high-resolution visualization of cardiac electric spatiotemporal dynamics

ALEXANDER ALVAREZ,^{1,2,*} ID CHET PRESTON,¹ TEODORO TRUJILLO,¹ CAMERON WILHITE,³ ALEX BURTON,¹ SONIA VOHNOUT,² AND RUSSELL S. WITTE^{1,2,3,4}

¹Department of Biomedical Engineering, University of Arizona, 1230 N Cherry Ave., Tucson, Arizona 85719, USA

²Electrosonix, LLC, 435 E 9th St., Tucson, Arizona 85705, USA

³Department of Medical Imaging, University of Arizona, 1230 N Cherry Ave., Tucson, Arizona 85719, USA

⁴James C. Wyant College of Optical Sciences, University of Arizona, 1630 E University Blvd., Tucson, Arizona 85719, USA

*Corresponding author: alexander.alvarez@email.arizona.edu

Received 14 September 2020; revised 14 November 2020; accepted 16 November 2020; posted 17 November 2020 (Doc. ID 410172); published 11 December 2020

Acoustoelectric cardiac imaging (ACI) is a hybrid modality that exploits the interaction of an ultrasonic pressure wave and the resistivity of tissue to map current densities in the heart. This study demonstrates for the first time *in vivo* ACI in a swine model. ACI measured beat-to-beat variability ($n = 20$) of the peak of the cardiac activation wave at one location of the left ventricle as $5.32 \pm 0.74 \mu V$, 3.26 ± 0.54 mm below the epicardial surface, and 2.67 ± 0.56 ms before the peak of the local electrogram. Cross-sectional ACI images exhibited propagation velocities of 0.192 ± 0.061 m/s along the epicardial–endocardial axis with an SNR of 24.9 dB. This study demonstrates beat-to-beat and multidimensional ACI, which might reveal important information to help guide electroanatomic mapping procedures during ablation therapy. © 2020 Optical Society of America

<https://doi.org/10.1364/AO.410172>

1. INTRODUCTION

Hybrid medical imaging technologies utilize two or more energy sources to create new forms of contrast for imaging. By fusing multiple datasets of anatomical and/or physiologic information, these hybrid modalities can help improve diagnosis or guide therapy. For example, photoacoustic imaging exploits the interaction between light, thermal energy, and acoustic energy to produce high-resolution images with both greater penetration than traditional optical methods and better contrast than ultrasound imaging. This study explores another hybrid modality that exploits the link between a pressure wave and the resistivity of tissue to produce images that can be used to map electrical activity in the body. Specifically, we demonstrate for the first time *in vivo* acoustoelectric cardiac imaging (ACI), which uses a focused ultrasound (US) beam to generate high-resolution 4D images of current densities in the heart, that could potentially help inform image-guided therapy of electrical diseases, such as cardiac arrhythmias.

A. Limitations with Standard Cardiac Mapping Technologies

Arrhythmias are electrical diseases of the heart that may result in severe morbidity and mortality [1]. If patients' arrhythmias

cannot be effectively managed with antiarrhythmic drugs, they are likely to undergo cardiac ablation, a treatment in which regions of tissue are burned to try to restore the heart's normal electrical rhythm. The gold standard for visualizing spatiotemporal dynamics of arrhythmias to guide ablation treatment is electroanatomic mapping (EAM). EAM systems fuse pre-procedural, high-resolution anatomical imaging obtained via computed tomography (CT) with local cardiac electrograms (EGMs) obtained by dragging intracardiac electrodes with interelectrode spacing $\sim 2\text{--}6$ mm along various locations in the heart [2,3].

However, EAM has two distinct disadvantages. First, there is a risk of harm to patients due to the invasive introduction of an electrophysiology recording catheter into the heart via the veins and due to exposure to ionizing radiation for pre-procedural CT and fluoroscopic guidance. Second, EAM can produce inaccurate maps that lead to poor patient outcomes after ablation due to long procedure durations (>2 h), the necessity for direct contact with convoluted anatomic structures, and difficulty in registering electrical maps to anatomical images [4]. This inaccuracy is compounded by the fact that EAM relies on contact electrodes that are unable to capture transmural electrical activation (i.e., the activation across the thickness of the wall of the heart), which can drive arrhythmias and affect the success

of ablation procedures. Other novel imaging technologies have been proposed to overcome limitations with conventional EAM. Electrical impedance tomography (EIT), which measures impedance after passing a small current through the tissue, can highlight potential substrate for electrical arrhythmias. Because EIT focuses on the conductivity of a tissue rather than the underlying current density, though, it is not capable of mapping the cardiac activation wave itself [5]. In this study, we describe *in vivo* ACI, a novel approach to image electrical propagation in the heart, which may overcome mapping errors present in standard methods for pre-ablation guidance in order to improve treatment outcomes for patients with advanced arrhythmias. ACI has been previously demonstrated in mapping the cardiac activation wave in *ex vivo* animal hearts; however, this study is the first to describe such mapping in an *in vivo* setting.

B. Acoustoelectric Cardiac Imaging

Acoustoelectric (AE) imaging exploits two physical principles, namely the AE effect and Ohm's law, to map electric currents in the body [6–10]. The AE effect is a modulation of the electrical resistivity $\rho_0(x, y, z)$ of a material with the application of ultrasonic pressure ΔP :

$$\Delta\rho = \rho_0 K_I \Delta P, \quad (1)$$

where $\Delta\rho(x, y, z)$ is the change in electrical resistivity and $K_I(x, y, z)$ is the AE interaction constant, which has been measured in cardiac tissue to be 0.1%/MPa [11].

In accordance with Ohm's law, when this resistivity change occurs in cardiac tissue where current is flowing, a radiofrequency voltage signal near the US carrier frequency will be produced and consequently sensed by one or more recording electrodes. This voltage signal $V_{AE}(x_1, y_1, z_1, t_{phys})$ is proportional to the local current densities $J_I(x, y, z, t_{phys})$ in the tissue (see Fig. 1) at the focal location of the propagating US wave with pressure amplitude P_0 . The general AE equation is given by

$$V_{AE} = \iiint [J_L \bullet J_I] [K_I \rho_0 P_0 b a] dx dy dz, \quad (2)$$

where $J_L(x, y, z)$ is the lead field (i.e., a vector representing the sensitivity distribution of the recording lead), $b(x-x_1, y-y_1, z)$ is the US beam pattern, and $a(t_{US}-z/c)$ is the US pulse waveform. t_{US} and t_{phys} indicate the US propagation time (in microseconds) and physiologic time (in milliseconds), respectively. Detailed derivations of the general AE equation have been previously described [12–14].

As indicated by Eq. (2) and demonstrated in several previous publications [15–17], the spatial resolution in ACI is determined primarily by the US focal size, which can be modeled through numerical simulations, directly measured with a commercial hydrophone, or approximated using ACI of a monopole point source (i.e., current generated by a thin stimulating electrode). Previous work has studied the resolution of different US arrays for AE imaging, including single elements with different center frequencies [15] and a 0.6 MHz array in a human head phantom [18].

Earlier ACI studies have successfully employed this theory and developed the US beamforming, signal acquisition systems, and data visualization tools to measure current densities

around electrically active imaging phantoms [15,17,19] and *ex vivo* Langendorff-perfused rat and rabbit hearts [12,20,21]. However, the use of electrical pacing and electromechanical uncouplers like 2,3-butanedione monoxime in these models and the lack of realistic electromagnetic interference from a live animal necessitate the use of *in vivo* models that better mimic the clinical setting.

C. Goals of the Study

The goal of this study was to demonstrate *in vivo* ACI for the first time in swine and assess the benefits and limitations of this new modality for mapping cardiac conduction. To accomplish this innovation, we developed instrumentation and methodology for *in vivo* mapping, including the first mobile cart for *in vivo* ACI, the use of a 0.6 MHz 2D array driven by a research US platform for sequence control and steering with high sensitivity, an interface for imaging the beating pig heart with appropriate grounding and improved electronics to minimize noise, and signal processing for characterizing the spatiotemporal dynamics of electrical activation. This proof-of-concept study is a critical leap forward toward clinical translation of ACI technology for real-time mapping of the human heart to help guide ablative treatment of arrhythmias.

2. METHODS

A. Animal Procedure

All animal procedures and euthanasia were approved by the Institutional Animal Care and Use Committee at the University of Arizona. A healthy male swine weighing 25 kg was placed under general anesthesia with isoflurane. A thoracotomy was performed with the swine in the supine position to expose the epicardium for imaging and electrophysiology. Vital signs, anesthesia, and analgesia were monitored for the duration of the procedure by trained veterinary staff.

B. Signal Acquisition

A 10-site catheter electrode array (ecoLasso catheter; Biosense Webster, Inc.; Irvine, CA) was placed on the left ventricle distal to the bifurcation with the diagonal branch (Fig. 1, top middle) to record low-frequency (LF, <10 kHz) bipolar cardiac EGMS and high-frequency (HF, >0.2 MHz) ACI signals. Electrical signals recorded on the catheter array were passed through a differential amplifier (DA1855; LeCroy Corp.; Chestnut Ridge, NY) and split into LF and HF components in a custom preamplifier; HF components of the signal had additional low-pass filtering <2.5 MHz. LF bipolar EGMS were acquired on a National Instruments DAQ (PXI-6289; National Instruments; Austin, TX) at 20 kHz; HF ACI signals were acquired on a fast acquisition board (PXI-5105; National Instruments; Austin, TX) at 10 MHz (Fig. 1).

For ACI, a custom 0.6 MHz 2D US matrix array with 126 elements (18 × 7) and a spatial resolution between 3 and 4 mm within the focal zone (~30–50 mm) [18] (fabricated by Sonic Concepts; Bothell, WA) was used. The US array was acoustically coupled to the epicardium using a waveguide adapter filled with acoustic coupling rubber ($c = 1449$ m/s, $\rho = 880$ kg/m³)

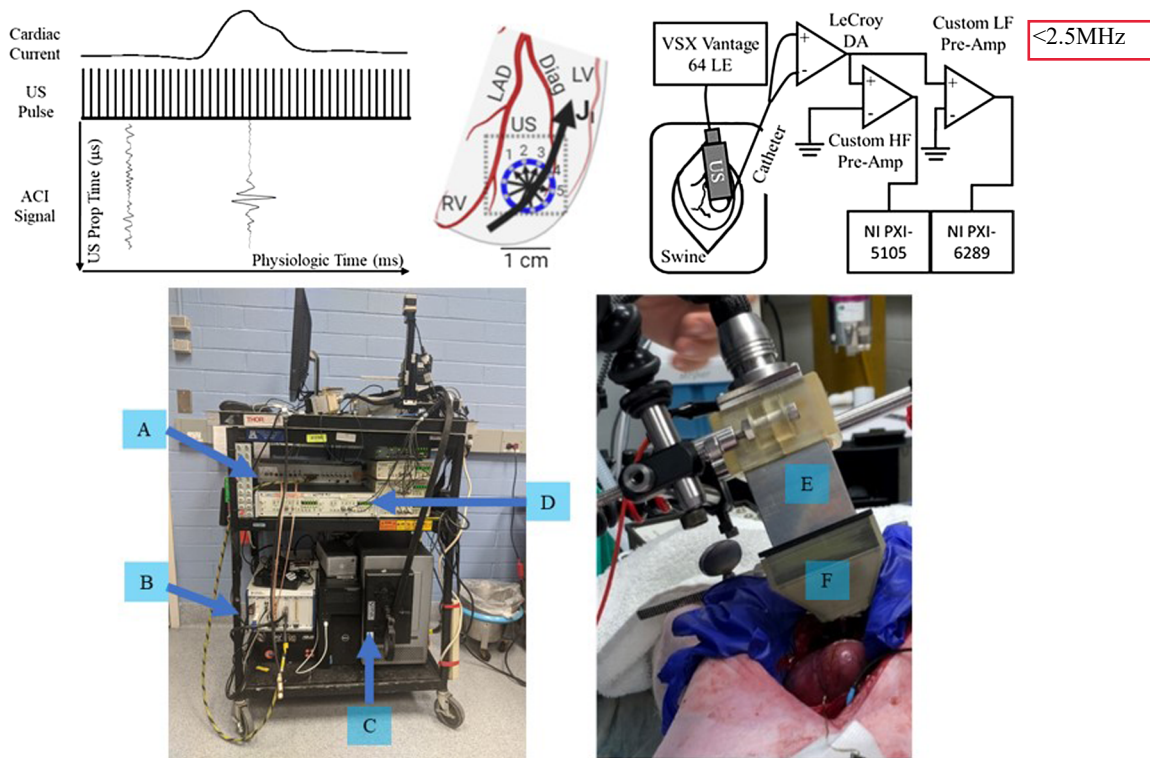


Fig. 1. Experimental setup for *in vivo* ACI in open chest swine heart model. (*Top left*) Timing of US pulses (pulse repetition frequency = 4 kHz) and data collection for ACI. Cardiac current (J_1) represents the current flow through the heart during cardiac activation (top middle panel). US propagation time in μs is converted to depth in mm via multiplication by the medium's speed of sound (1.5 mm/ μs). (*Top middle*) Orientation of the bipolar leads and active area of the 2D US matrix array on the heart (LAD, left anterior descending artery; Diag, diagonal artery; US, ultrasound array; LV, left ventricle; RV, right ventricle; 1–5, bipolar leads of catheter electrode). (*Top right*) Connection diagram of hardware for *in vivo* ACI for one of the five leads in top middle panel. LF bipolar EGMs had a gain of 80, whereas HF AE signals had a gain of 4400 (DA, differential amplifier; HF, high frequency; LF, low frequency). (*Bottom left*) ACI instrumentation on mobile ACI cart. *A*: custom LF and HF pre-amplifier; *B*: NI PXI-5105 & PXI-6289; *C*: Verasonics Vantage 64LE; *D*: LeCroy differential amplifier. (*Bottom right*) US array in median sternotomy of swine; *E*: custom 2D US array; *F*: acoustic adapter filled with acoustic coupling rubber.

(Gelatin #0, Humimic Medical; Greenville, SC), and the adapter was pressed against the catheter electrodes (Fig. 1). Short US pulses were delivered by a commercial US platform (Vantage 64LE; Verasonics, Inc.; Kirkland, WA) at 4 kHz pulse repetition frequency, giving a temporal sampling of 250 μs . The maximum ultrasound exposure was near safe levels for diagnostic imaging (i.e., mechanical index = 2.54; spatial-peak temporal-average intensity [I_{spa}] = 753 mW/cm²). Depth versus time ACI maps were collected in real time. 2D, 3D, and 4D ACI scans with multiple beats and/or azimuthal/elevational beam positions took 2.5 min., 20.5 min, and 47.25 min., respectively. Acquired data were processed and analyzed offline for display.

C. Signal and Image Processing

ACI data consisted of five dimensions (US propagation time \times US pulses \times number of cardiac cycles \times apicobasal US beam positions \times recording channels), which were used to produce images in Fig. 2.

Retrospective gating of the EGM was performed to facilitate averaging over multiple cardiac cycles. The depolarization spike of each recorded EGM was cross-correlated with a template EGM waveform to align multiple heart beats before averaging.

To quantify spatiotemporal dynamics of electrical activation that might aid in guiding ablation therapy, three quantities were extracted from the peak ACI magnitude and spatial location of peak activation for each frame. First, isochrones maps, which display areas of tissue that simultaneously activate by assigning those areas of tissue a color, were generated by determining the peak time delay of the ACI signal from the EGM at each pixel in a cross-sectional ACI image. Second, voltage maps, which exhibit areas of tissue that are less conductive (e.g., scar tissue in non-healthy models) that may sustain arrhythmias, were generated by determining the global ACI signal maximum at each pixel in an ACI cross-sectional image during the entire cardiac cycle. Third, propagation velocities, which could be used to illustrate conduction pathways in the tissue, were determined using the cardiac vectorgram. This vectorgram depicted the location of peak activation for each frame in the cardiac cycle as a point on a 2D scatter plot. To calculate propagation velocity, a linear fit of the cardiac vectorgram over several frames during peak activation was taken.

For signal-to-noise ratio (SNR) calculations, a region of interest was selected between –1 mm and 7 mm from the epicardial surface. Signal measurements were taken from a single ACI depth line 2 ms prior to the peak of the LF EGM (during

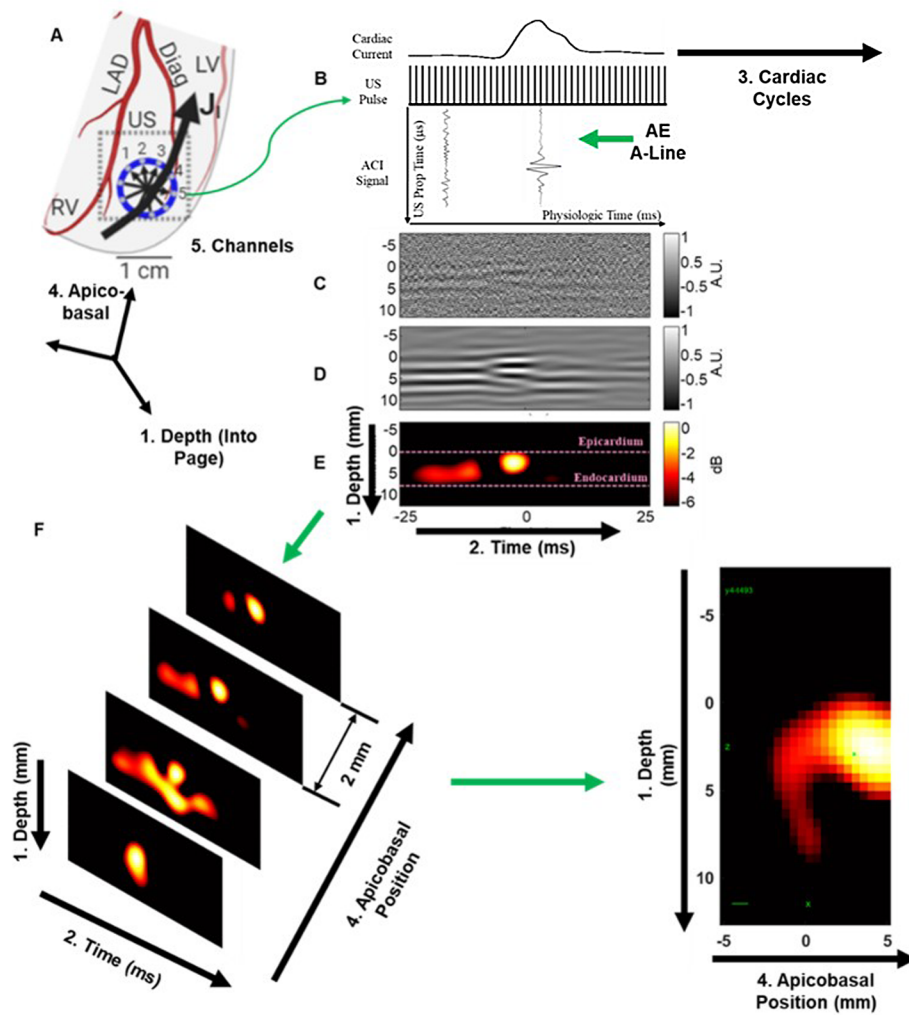


Fig. 2. ACI data collection and image formation. **A:** Schematic of ACI acquisition with three of the five dimensions shown at a single time point. **B:** To form raw ACI images (depth versus time), AE A-lines, which display the amplitude of the AE signal against US propagation time for each US pulse, were stacked along the physiologic time axis. **C:** Stacked AE A-lines were assigned color values based on the amplitude of the signal. **D:** Raw 2D ACI signals were bandpass filtered between 0.3 and 0.9 MHz along the US propagation axis consistent with the bandwidth of the custom US array. Signals were then bandpass filtered along the physiologic time axis. **E:** Magnitude ACI images were determined from the absolute value of the Hilbert transformed ACI signals, which were proportional to the amplitude of the local current densities **F:** To form cross-sectional ACI images (i.e., ACI B-mode), which demonstrate the 2D spatial extent of activation at a given time point in the cardiac cycle, depth versus time images (averaged over 15 consecutive beats per depth line) were stacked along the azimuthal US beam dimension. A median filter was then applied to the cross-sectional images before interpolation. Additionally, ACI cine-loops exhibited changes in the magnitude of the cross-sectional image over the cardiac cycle.

depolarization). Noise measurements were taken from an ACI depth line 125 ms after the peak of the LF EGM (i.e., during diastole after cardiac motion occurred).

3. RESULTS

ACI depth versus time images (Fig. 2E) illustrate the temporal dynamics of transmural cardiac activation (over 15 consecutive beats). Variability in cardiac activation and the effect of averaging was visualized and measured (Fig. 3). ACI images exhibited a peak signal of $5.32 \pm 0.74 \mu\text{V}$, $3.26 \pm 0.54 \text{ mm}$ below the epicardial surface, and $2.67 \pm 0.56 \text{ ms}$ before the peak of the LF EGM over 20 beats. This depolarization peak can be seen in the line profiles (Fig. 3, left column).

Representative cross-sectional ACI images (Fig. 2F) demonstrated 2D activation at a single time point in the cardiac cycle. The propagation of the cardiac activation wave was visualized by displaying cross-sectional images at multiple time points (Fig. 4 and Supp. Fig. 1). The FWHMs of the peak activation (-2 ms before the peak of the EGM) were 6.53 mm and 6.43 mm in the depth and apicobasal directions, respectively. The SNR for the peak frame in these images was 24.9 dB .

The effect of averaging multiple beats for each vertical line of a cross-sectional ACI image was also determined (Fig. 5). While a single beat at each vertical line resulted in a root-mean-squared (RMS) signal of $2.98 \pm 0.35 \mu\text{V}$, an RMS noise of $0.58 \pm 0.23 \text{ nV}$, and an SNR of $14.8 \pm 3.56 \text{ dB}$ (across 20 beats), averaging over 20 beats for each vertical line resulted in

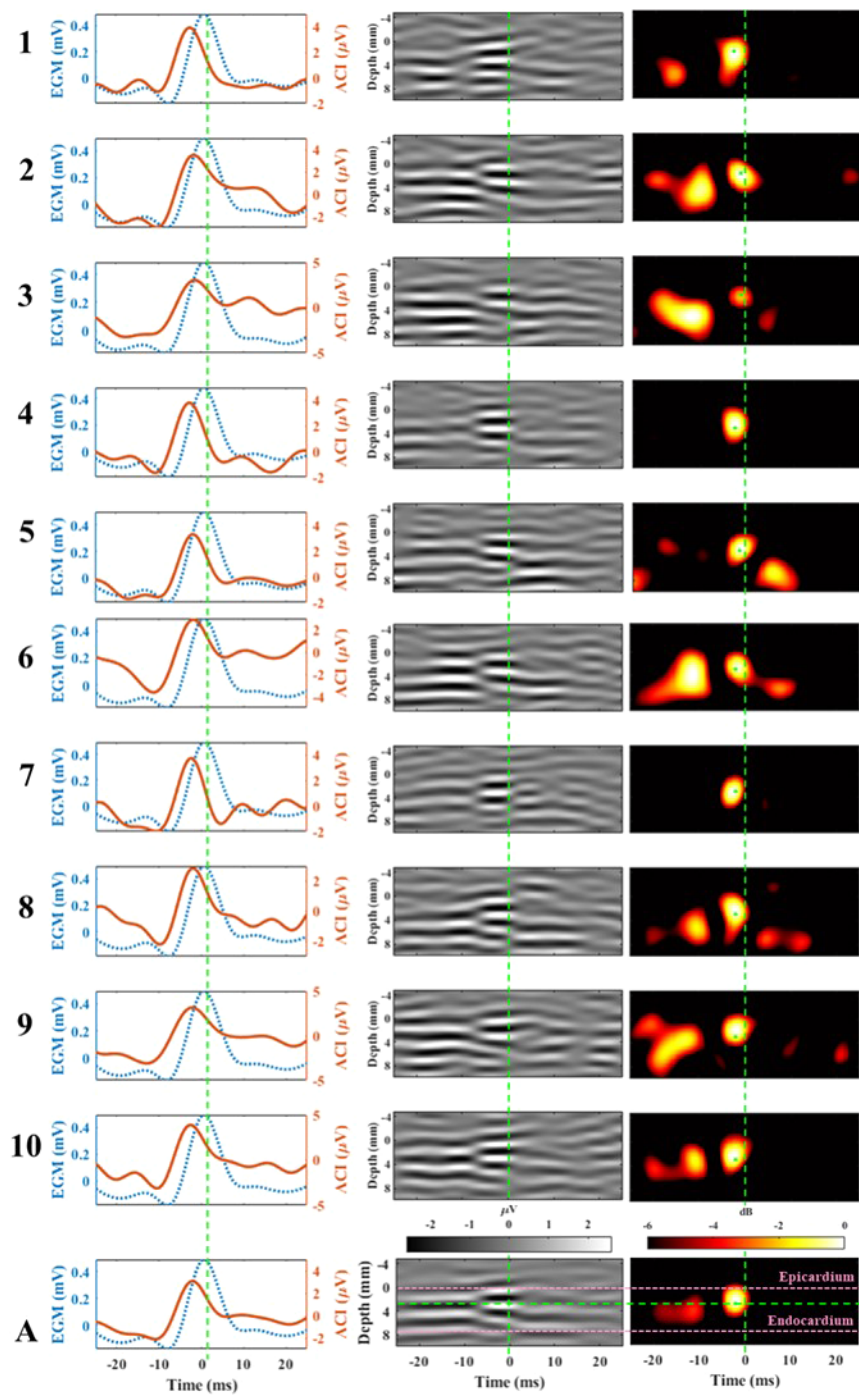


Fig. 3. Beat-to-beat variability using *in vivo* ACI of the swine LV. (*Left column*) Physiologic timeline of filtered AE signals at 3 mm below the epicardial surface (denoted by horizontal green line in bottom image). (*Middle and right column*) Phase and amplitude ACI (middle column) and magnitude ACI (right column) for 10 consecutive beats and average of all 10 beats (A, bottom). Epicardial (depth = 0 mm) and endocardial (depth = 7.8 mm) surfaces are marked with a pink dashed line. Time denotes peak of the EGM indicated by the vertical dashed green line in each column. All signals are measured from Lead 2 in Fig. 2A.

an RMS signal of 2.92 μ V, RMS noise of 0.28 nV, and an SNR of 24.9 dB.

Spatiotemporal dynamics were drawn from cross-sectional ACI to produce global voltage and isochrone maps (Fig. 6). Figure 6 also presents a cardiac vectorgram, indicating spatiotemporal propagation in the transmural and apicobasal axes

of the peak signal within a 5.75 ms window around the peak EGM.

Propagation velocity was calculated from the slope of the best fit line through the peak activation position versus time plots (Fig. 7). The mean and standard deviation of the propagation

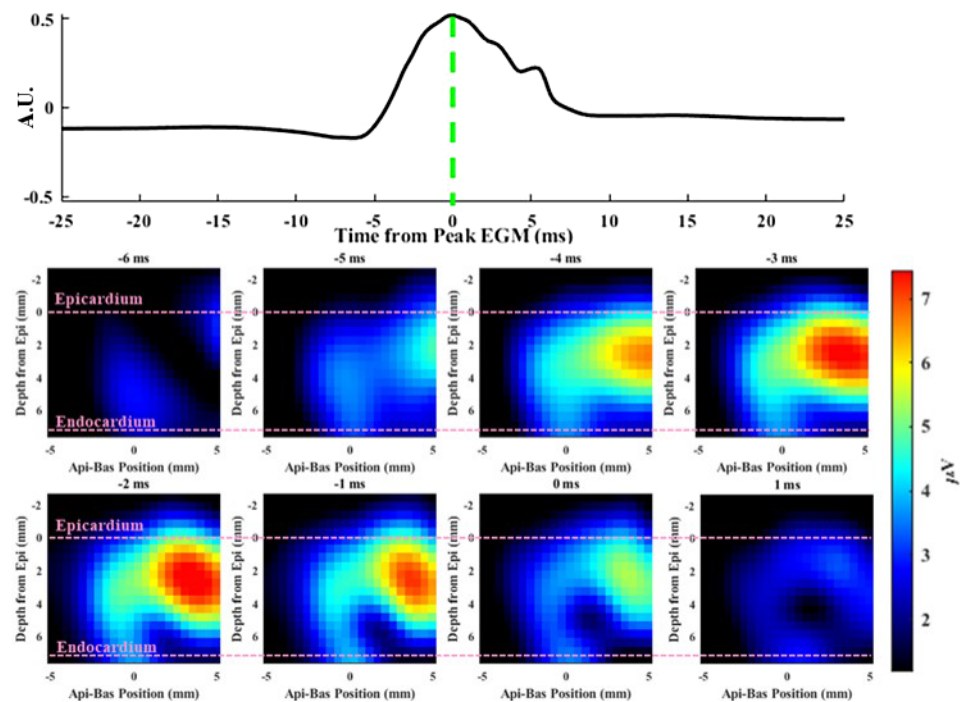


Fig. 4. ACI cross sections during peak activation in swine LV. (*Top*) Bipolar EGM obtained from Lead 2 (depicted in Fig. 2A). Vertical dashed line represents peak of the EGM ($t = 0$ ms). (*Bottom*) Cross-sectional ACI displayed on a linear scale demonstrating propagation of the current along the apicobasal and transmural axes. Pink dashed lines mark the endocardium and epicardium.

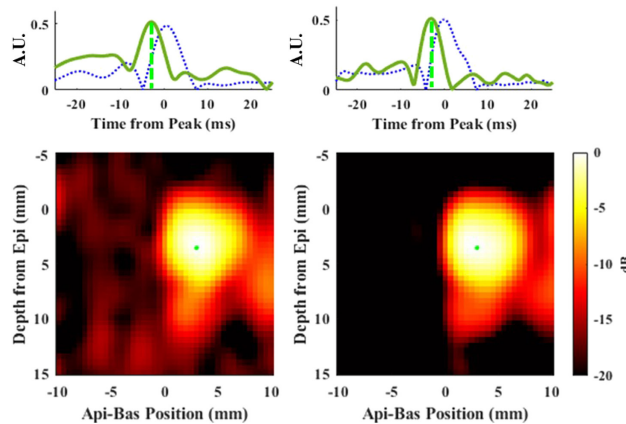


Fig. 5. Image quality comparing ACI for a single beat versus an average of 20 beats at each depth line. (*Top*) Normalized physiologic time ACI line profile (green) taken at the green pixel in the bottom ACI images along with filtered EGM (dashed blue). A similar line profile can be taken at every pixel in the image. (*Bottom left*) Cross-sectional ACI 3 ms prior to the peak of the EGM (dashed vertical green line) with a single beat displayed for each depth line. (*Bottom right*) Cross-sectional ACI at the same time point after averaging 20 beats together at each depth line.

velocity over 20 beats along the epicardial–endocardial axis was 0.192 ± 0.061 m/s.

4. DISCUSSION

This study demonstrated *in vivo* mapping of the spatiotemporal dynamics in a single swine heart using ACI technology for the

first time. Images (Figs. 2 and 3) revealed strong associations in time with EGMs measured directly from the epicardium. The slight delay between the peak ACI signal and the peak EGM (Figs. 3 and 5) may be explained by the sifting property of ACI, wherein activation information is only obtained at the focal position of the US beam (~ 3.5 mm wide). Whereas the EGM represents the integration of all activation in the 15 mm between the two recording electrodes, ACI captures local activation on a finer scale determined by the location of the US beam. This study also demonstrated that single beat electrical dynamics and beat-to-beat variability can be captured (14.8 ± 3.56 dB) (Figs. 3 and 5). ACI captured both a consistent depolarization peak across beats and mapped the variability in early onset activation that occurred before the peak ACI signal, exhibiting a peak signal of 5.32 ± 0.74 μ V, 3.26 ± 0.54 mm below the epicardial surface, and 2.67 ± 0.56 ms before the EGM. This feature of ACI is especially powerful as it would allow physicians to tune processing depending on the specific spatiotemporal dynamics they may be looking for. For example, when using ACI to detect arrhythmias that have transient appearances, a single-beat, high-sensitivity approach could be used to visualize beat-to-beat variability in real time and capture the higher-frequency components present in many complex arrhythmias [22]. Alternatively, when using ACI to map activation in areas of weaker electrical signaling (e.g., myocardial scar), an approach employing averaging across multiple beats could be employed to ensure signal detection with higher SNR and/or spatial resolution.

In addition to fast temporal dynamics and beat-to-beat variability, we also described the ability of ACI to capture electrical activity consistent with the depolarization of cardiac muscle cells

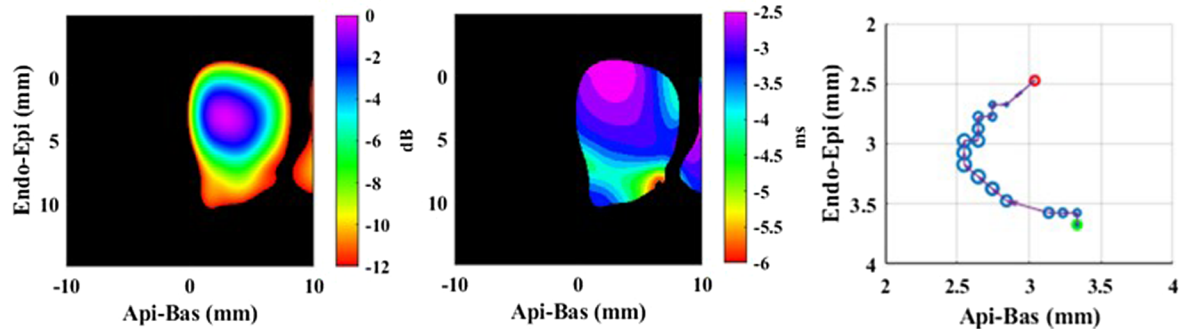


Fig. 6. Quantifying spatiotemporal dynamics during cardiac activation. (*Left*) ACI voltage map displays the global peak signal at each pixel across all frames. (*Middle*) Isochrone map displays the time of ACI activation relative to the peak of the EGM waveform (masked above a threshold of -6 dB), illustrating propagation along the apicobasal and epicardial/endocardial axes. (*Right*) Vectorgram displays the spatial propagation of the peak signal for each frame starting at $t = 5.75\text{ ms}$ before the peak of the EGM (green circle) and extending to the peak EGM (red circle; i.e., $t = 0\text{ ms}$). The size of the markers is weighted according to the magnitude of the ACI signal.

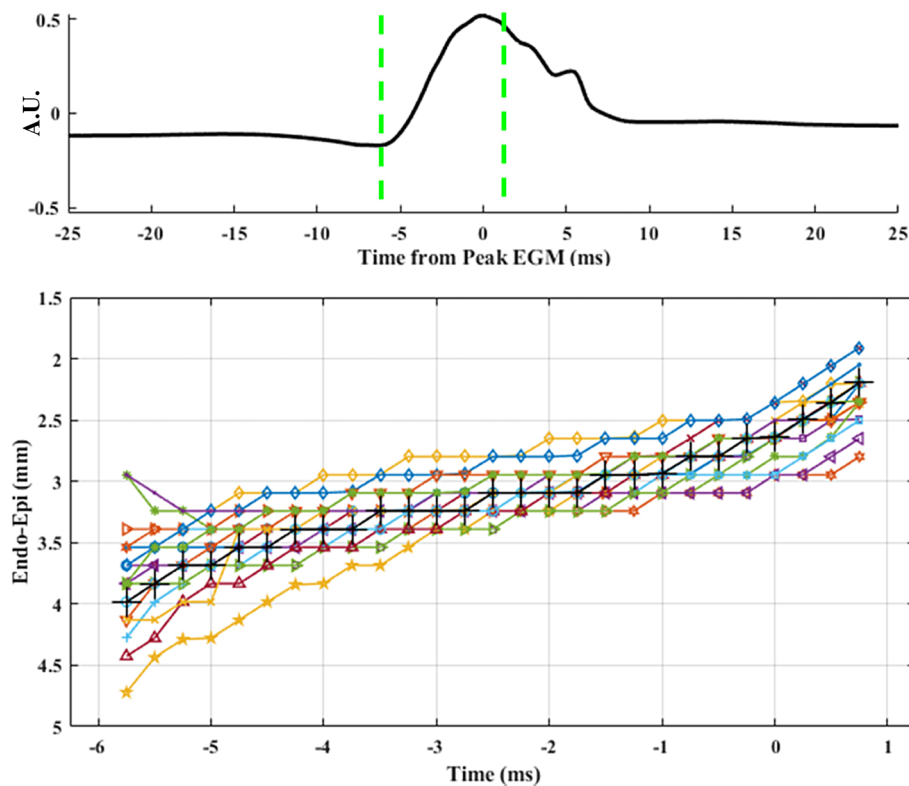


Fig. 7. Location of peak activation versus time from the peak EGM along the depth axis for 20 consecutive beats. Green dashed line in the EGM represents the time window for mapping peak activation. Whereas each symbol represents propagation for a single beat, the large black crosses denote the average over all beats ($n = 20$). These data were used to calculate propagation velocities.

spread across the epicardium, myocardium, and endocardium (Figs. 2–4). ACI delineated such 2D dynamics with a FWHM of 6.53 mm and 6.43 mm in the axial and lateral dimensions, respectively. This FWHM represents a combination of the spatial resolution of the ACI system using the 0.6 MHz array ($\sim 3\text{ mm}$ [23]) and the underlying spatial extent of the cardiac activation wavefront (measured to be 2–10 mm in previous work [24]). Further improvements to spatial resolution can be achieved by increasing the frequency of the US array [20,25]. ACI was also able to capture transmural propagation dynamics

in real time (Fig. 7), demonstrating an endocardial to epicardial propagation of $0.192 \pm 0.061\text{ m/s}$; this is especially important, as transmural abnormalities due to scar tissue and electrical dissociation of the endocardium and epicardium are considered to be one of several factors that may cause ventricular arrhythmias [26,27]. Along with normal physiologic variations in electrical signal propagation, rotation of the US probe with respect to the apical-basal propagation axis may have led to errors in calculating conduction velocity along this axis. However, by steering the beam in the azimuthal and elevational directions, volumetric

views of the cardiac activation wave would be possible, thereby eliminating this source of variability.

Finally, in this study, isochrone and voltage maps were generated from ACI maps (Fig. 6). Such images could be used to describe cardiac activation and identify the origin of arrhythmias during ablation therapy as is currently performed with gold standard EAM systems [2]. Importantly, unlike in EAM, ACI voltage maps correspond directly to cardiac currents rather than potentials, which more directly reflect the flow of electrical activity through cardiac tissue, allowing for improved scar mapping. However, the sensitivity distribution of the recording leads [see Eq. (2)] also serves as a scaling factor for the detected signal at each recording site, which leads to inaccuracies. To help correct for lead field effects, it is possible to use multiple recording channels for ACI and reconstruct the underlying current densities by solving an inverse problem [14,17]. The isochrone map and vectorgram in Fig. 6 exhibit propagation from the endocardium to the epicardium and from apex to base consistent with normal cardiac electrophysiology [28]. Alterations in isochrones could reveal the presence of multiple ectopic arrhythmia sources, which could be captured by ACI at high spatial and temporal resolution.

A. Limitations

There are three major limitations with this study. First, due to the relatively low AE signal strength ($<6 \mu\text{V}$), we relied on an open-chest model with electrodes placed in contact with the epicardium. However, intracardiac ACI is also possible [29], which would be more relevant for interventional procedures consistent with EAM. Ongoing studies will extend this work to the minimally invasive setting in which intracardiac catheter electrodes will be used for ACI. Second, due to the use of focused US imaging, the field-of-view was restricted to the left ventricle. Because ACI is limited by the number of US beams per cardiac cycle, there is an inherent trade-off between the spatial and temporal sampling (or frame rate) and field-of-view. This is common in 3D echocardiography except ACI requires only one-way travel of the US beam, enabling more beams per cycle.

Although this study was limited to a single swine, it was the first to demonstrate *in vivo* ACI and beat-to-beat mapping on the millimeter and millisecond scale, which are major breakthroughs in the development of ACI technology. Moreover, we presented data from multiple scans in the same pig and report low beat-to-beat variability in key ACI signal metrics (latency, peak amplitude, conduction velocity, and propagation). Ongoing and future ACI experiments in additional swine will assess the reliability and reproducibility of *in vivo* ACI and estimate physiologic variability of the cardiac activation wave across animals.

B. Conclusion

In summary, this is the first study to demonstrate *in vivo* ACI for capturing complex, beat-to-beat spatiotemporal dynamics associated with cardiac electrical activation in an open-chest swine model with high spatial (3 mm) and temporal resolution ($<1 \text{ ms}$). The excellent spatiotemporal resolution inherent in ACI along with its ability to capture beat-to-beat dynamics

across the myocardium unlock its potential to improve guidance for ablation procedures and establishes an optimistic foundation to build more effective treatments for cardiac arrhythmias.

Funding. National Institutes of Health (SBIR R43HL144327, T32HL007955, T32M132008, T35HL007479).

Acknowledgment. We thank Dr. Talal Moukabary, MD, for feedback in interpreting the swine data. We also thank Pier Ingram and the Center for Gamma Ray Imaging for providing the custom 3D printed parts. We would also like to acknowledge Alice McArthur and Debbie Mustacich for their assistance with the animal preparation and experiments.

Disclosures. Sonia Vohnout and Russell Witte have a financial interest in ElectroSonix, which sponsored this study through the parent Phase 1 NIH Award (R43HL144327).

REFERENCES

1. M. J. Janse and M. R. Rosen, "History of arrhythmias," in *Basis and Treatment of Cardiac Arrhythmias*, Handbook of Experimental Pharmacology (Springer, 2006), pp. 1–39.
2. D. Bhakta and J. M. Miller, "Principles of electroanatomic mapping," *Indian Pacing Electrophysiol. J.* **8**, 32–50 (2008).
3. Medical Advisory Secretariat, "Advanced electrophysiologic mapping systems," *Ont. Health Technol. Assess. Ser.* **6**, 1–101 (2006).
4. A. Grace, S. Willems, C. Meyer, A. Verma, P. Heck, M. Zhu, X. Shi, D. Chou, L. Dang, C. Scharf, G. Scharf, and G. Beatty, "High-resolution noncontact charge-density mapping of endocardial activation," *JCI Insight* **4**, e126422 (2019).
5. P. Grasland-Mongrain and C. Lafon, "Review on biomedical techniques for imaging electrical impedance," *IRBM* **39**, 243–250 (2018).
6. R. S. Witte, R. Olafsson, S.-W. Huang, T. L. Hall, and M. O'Donnell, "Acoustic sensor utilizing acoustoelectric effect," U.S. patent 8,427,906 (23 April 2013).
7. R. S. Witte, C. Ingram, Q. Li, and Y. Qin, "Acoustoelectric image-guided therapy," U.S. patent 3,463,070 (4 October 2019).
8. R. S. Witte, Y. Qin, M. O'donnell, Z. Xu, and C. Ingram, "Handheld ultrasound transducer array for 3D transcranial and transthoracic ultrasound and acoustoelectric imaging and related modalities," U.S. patent WO/2019/051216 (14 March 2019).
9. R. S. Witte, R. Olafsson, and M. O'Donnell, "High-resolution mapping of bio-electric fields," U.S. patent 8,057,390 (15 November 2011).
10. R. S. Witte, C. Preston, Y. Qin, C. Ingram, and A. Burton, "Imaging electrical current patterns generated by a medical device," World Intellectual Property Organization patent WO2019051223A1 (14 March 2019).
11. Q. Li, R. Olafsson, P. Ingram, Z. Wang, and R. Witte, "Measuring the acoustoelectric interaction constant using ultrasound current source density imaging," *Phys. Med. Biol.* **57**, 5929–5941 (2012).
12. B. Berthon, P.-M. Dansette, M. Tanter, M. Pernot, and J. Provost, "An integrated and highly sensitive ultrafast acoustoelectric imaging system for biomedical applications," *Phys. Med. Biol.* **62**, 5808–5822 (2017).
13. C. Preston, W. S. Kasoff, and R. S. Witte, "Selective mapping of deep brain stimulation lead currents using acoustoelectric imaging," *Ultrasound Med. Biol.* **44**, 2345–2357 (2018).
14. R. Yang, X. Li, A. Song, B. He, and R. Yan, "A 3-D reconstruction solution to current density imaging based on acoustoelectric effect by deconvolution: a simulation study," *IEEE Trans. Biomed. Eng.* **60**, 1181–1190 (2013).

15. Y. Qin, Z. Wang, P. Ingram, Q. Li, and R. S. Witte, "Optimizing frequency and pulse shape for ultrasound current source density imaging," *IEEE Trans. Ultrason. Ferroelectr. Freq. Control* **59**, 2149–2155 (2012).
16. Z. H. Wang, R. Olafsson, P. Ingram, Q. Li, Y. Qin, and R. S. Witte, "Four-dimensional ultrasound current source density imaging of a dipole field," *Appl. Phys. Lett.* **99**, 113701 (2011).
17. R. Olafsson, R. S. Witte, S.-W. Huang, and M. O'Donnell, "Ultrasound current source density imaging," *IEEE Trans. Biomed. Eng.* **55**, 1840–1848 (2008).
18. Y. Qin, P. Ingram, Z. Xu, M. O'Donnell, and R. S. Witte, "Performance of a transcranial US array designed for 4D acoustoelectric brain imaging in humans," in *IEEE International Ultrasonics Symposium (IUS)* (2017), pp. 1–4.
19. C. Preston, A. M. Alvarez, A. Barragan, J. Becker, W. S. Kasoff, and R. S. Witte, "High resolution transcranial acoustoelectric imaging of current densities from a directional deep brain stimulator," *J. Neural Eng.* **17**, 016074 (2020).
20. Y. Qin, Q. Li, P. Ingram, C. Barber, Z. Liu, and R. S. Witte, "Ultrasound current source density imaging of the cardiac activation wave using a clinical cardiac catheter," *IEEE Trans. Biomed. Eng.* **62**, 241–247 (2015).
21. B. Berthon, A. Behagel, P. Mateo, P.-M. Dansette, H. Favre, N. Ialy-Radio, M. Tanter, M. Pernot, and J. Provost, "Mapping biological current densities with ultrafast acoustoelectric imaging: application to the beating rat heart," *IEEE Trans. Med. Imaging* **38**, 1852–1857 (2019).
22. J. Morellato, W. Chik, M. A. Barry, J. Lu, A. Thiagalingam, P. Kovoov, and J. Pouliopoulos, "Quantitative spectral assessment of intracardiac electrogram characteristics associated with post infarct fibrosis and ventricular tachycardia," *PLoS One* **13**, e0204997 (2018).
23. A. Barragan, C. Preston, A. Alvarez, C. P. Ingram, T. Kanti Bera, and R. S. Witte, "4D transcranial acoustoelectric imaging of current densities in a human head phantom," in *IEEE International Ultrasonics Symposium (IUS)* (2019), pp. 2049–2051.
24. G. Arisi, E. Macchi, S. Baruffi, S. Spaggiari, and B. Taccardi, "Potential fields on the ventricular surface of the exposed dog heart during normal excitation," *Circ. Res.* **52**, 706–715 (1983).
25. A. Alvarez, J. Ferng, C. Preston, C. Ingram, and R. S. Witte, "Effects of ultrasound frequency and beam pattern on acoustoelectric cardiac imaging," presented at IEEE International Ultrasonics Symposium, Kobe, Japan, 22–25 October 2018.
26. F. G. Akar and D. S. Rosenbaum, "Transmural electrophysiological heterogeneities underlying arrhythmogenesis in heart failure," *Circ. Res.* **93**, 638–645 (2003).
27. C. Antzelevitch and A. Burashnikov, "Overview of basic mechanisms of cardiac arrhythmia," *Card. Electrophysiol. Clin.* **3**, 23–45 (2011).
28. R. Mačiškiienė, I. Martišienė, A. Navalinskas, R. Vosyliūtė, R. Treinys, B. Vaideytė, R. Benetis, and J. Jurevičius, "Evaluation of excitation propagation in the rabbit heart: optical mapping and transmural microelectrode recordings," *PLoS ONE* **10**, e0123050 (2015).
29. Q. Li, Y. Qin, P. Ingram, R. Witte, and Z. Wang, "Ultrasound current source density imaging using a clinical intracardiac catheter," in *IEEE International Ultrasonics Symposium* (2011), pp. 704–707.